Proton Radiography

D. A. Clark, C. J. Espinoza, J. J. Gomez, G. E. Hogan, F. E. Merrill, B. Montoya, C. L. Morris, M. M. Murray, and A. Saunders (P-25); K. R. Alrick, N. T. Gray, M. Y. Hockaday, N. S. King, K. B. Morley, P. D. Pazuchanics, and M. D. Wilke (P-23); D. J. Clark (P-22); J. B. McClelland (P-DO); A. R. Mathews and J. S. Sarracino (X-4); J. Favorite, A. B. Kaye, and J. D. Zumbro (X-5); K. L. Buescher, D. J. Cagliostro, J. E. Pearson, G. L. Sandine, and K. R. Vixie (X-8); W. J. Deninger, E. N. Ferm, and K. H. Mueller (DX-3); C. T. Mottershead (LANSCE-1); E. Ables, M. B. Aufderheide, P. D. Barnes, Jr., E. P. Hartouni, H.-S. Park, R. A. Soltz, A. S. von Wittenau, and D. M. Wright (LLNL); S. D. Gardner, N. S. Khalsa, R. P. Liljestrand, D. V. Morgan, R. T. Thompson, T. W. Tunnell, and A. Whiteson (BN LA); R. Prigl and J. Scaduto (BNL CAD); G. A. Greene and A. L. Hanson (BNL ES&T); and P. Robertson (AWE)

Introduction

Over 100 years ago Wilhelm Roentgen discovered x-rays and utilized their ability to penetrate matter to look within a living human body (his wife's hand). Since that time x-radiography has been used for a number of applications where the inside of an object must be viewed. A source of x-rays, usually produced by the interactions of an energetic electron beam with a metal anode, is directed at an object and the transmitted beam is measured on a detector located behind the object. The detector produces an image of the shadow cast by differential absorption of the material that composes the object.

Late time hydrotest radiography is the experimental cornerstone of the stockpile stewardship program, an important part of the Los Alamos National Laboratory (Laboratory) mission. In these experiments the fissionable material in a weapon primary is replaced by simulants and the material densities and flow, thus the name hydrotest, are studied in explosive driven systems. Although these experiments produce no nuclear yield, they can provide data on how material properties influence the progression of a nuclear weapon up until the time when nuclear process began to dominate the dynamics. In these experiments data and models developed in science experiments can be integrated and tested, engineering changes can be tested, and aging effects measured in systems that are as close to those obtained in a nuclear explosion as can be obtained under a comprehensive test ban treaty. Until recently the only late time diagnostic of the compressed primary in a hydrotest has been flash x-radiography. Considerable resources have been expended to explore the limits of dose and spot size in order to provide the best possible data. It is becoming clear that these data are limited by the physics of electron and gamma ray interactions with matter, and do not meet the requirements of stockpile certification.

About six years ago, medium-energy proton beams were recognized to have a mean free path (the mean length that particles travel before interacting in material) much better matched to diagnose hydrotest systems than x-rays. Over the last six years, the techniques needed to perform dynamic experiments using proton beams have been developed, and proton radiography has been demonstrated to provide data on dynamic systems that is far superior to that which can be obtained with flash x-rays, even for thin systems.

Dynamic experiments using the 800 MeV protons have become routine part of the Los Alamos Neutron Science Center (LANSCE) program at the Laboratory. In addition we have performed experiments at using 24 GeV protons from the Alternating-Gradient Synchrotron (AGS) accelerator at Brookhaven National Laboratory (Brookhaven) using static test objects to clearly show some of the advantages of proton radiography when compared with the Dual-Axis Radiographic Hydrotest (DARHT) facility, the state-of-the-art flash x-ray machine.

Transmission Radiography

In transmission radiography, the transmitted flux through an object is used to measure its areal density. The transmission, $t_\lambda = N/N_0$, is given in terms of the path length l through the object and the mean free path λ by:

$$t_\lambda = e^{-\frac{l}{\lambda}} \qquad (1)$$

Where N_0 and N are the incident and transmitted number of particles respectively. Transmission is measured as a function of position and inverted to calculate the thickness of the object as:

$$l = -\lambda \ln(t_\lambda) \qquad (2)$$

Here, λ, is given by:

$$\lambda = \frac{1.}{\rho\sigma}, \qquad (3)$$

Equations 1 and 2 assume that the material can be described with a constant λ. When this is not the case (*e.g.*, for bremstrahlung x-rays where the x-rays are produced into a continuous energy spectrum) Equation 1 needs to be convoluted with the energy spectrum. In this case the solution is more difficult to obtain.

The uncertainty in the path length can be calculated, assuming Poisson statistics for the transmitted beam, by taking the derivative of Equation 2 with respect to the transmitted flux and propagating the error in N to l. This gives

$$\Delta l = \frac{\lambda}{\sqrt{N}} = \frac{\lambda}{\sqrt{N_0}} e^{\frac{l}{2\lambda}}. \qquad (4)$$

Setting the derivative of Equation 4 to zero and solving for λ gives the optimum mean free path, $\lambda = l/2$, for minimizing the uncertainty, Δl, for a fixed incident particle budget, N_0.

Thick object radiography is driven by this result. The large machines that have been built for hydrotest radiography in the U.S. (DARHT, PHERMEX, and FXR) are optimized for producing 4 MeV x-rays, because this is the energy where the x-ray mean free path peaks in high-Z materials.

Comparing x-ray and proton doses requires taking into account a number of experimental effects shown in Table 1. These include effective vs actual dose for x-rays, geometry, practical detector efficiencies, and the effect of containment windows. The results of simulated radiographs, neglecting backgrounds bluing and other effects is shown in Figure 1. The comparison assumes doses of 10^{11} protons with a width of 2.5 cm and 500 rad at one meter for x-rays. These are the doses that have been obtained at the AGS proton accelerator and at DARHT respectively.

These simulations demonstrate the dramatic advantage obtained from protons for objects thicker than about 200 gm/cm^2. The large fluctuations observed near the thick end of the step wedge in the x-ray analysis result from pixels in which there are zero detected x-rays, and thus no information on the thickness. These simple predictions are supported by measurements on classified test objects.

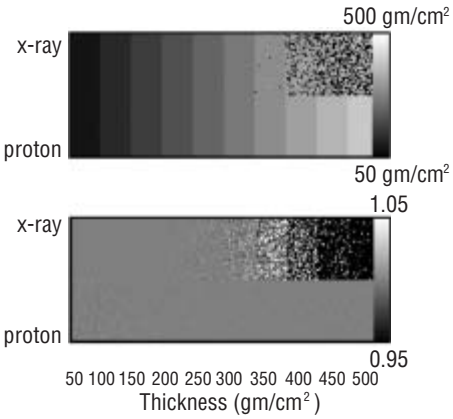

Figure 1. Top panel: Image of inferred areal densities using equation 2 from simulated radiographs made with x-rays (top half of image) and protons (bottom half of the image) for a uranium step wedge. Bottom panel: The ratio if the inferred densities to the actual densities. The pixel size is 0.5 mm.

Table 1: Correction Factors Applied to the Proton X-Ray Comparison

	Correction Factors	
	X-Ray	Protons
Useful Flux/Total Flux	0.3	1
DQE	0.3	0.4
Distance to Source	$(1./1.2)^2$	1
Absorption in Windows	$\exp^{-13.7/32.1}$	$\exp^{-54.86/106.4}$
Total	0.040787484	0.238856522

Charged-Particle Radiography

The invention that allows charged-particle radiography to be useful on thick objects is the idea that the transmitted beam can be focused in a magnetic lens creating an image with a long standoff from the dynamic object. The ability to focus both the beam and transmitted flux gives flexibility to charge particle radiography that doesn't exist for x-radiography.

A simple model for proton or other charged particle radiography can been obtained by assuming that nuclear scattering results in the removal of beam particles from the transmitted flux described by Equation 1 and that Coulomb scattering can approximated by assuming transmitted particles are scattered into a Gaussian shaped angular distribution. In this approximation integration of the angular distribution between limits imposed by angle collimators at the Fourier points in the lenses results in closed form expressions for the transmission. A beam transmitted though an object acquires an angular spread,

$$I(\theta) = \frac{1}{\pi\theta_0} e^{\frac{-\theta^2}{2\theta_0^2}} \qquad (5)$$

Where,

$$\theta_0 = \frac{14.1}{p\beta}\sum_i \frac{\rho_{Ai}}{X_i} \qquad (6)$$

Here p is the beam momentum, $\beta = v/c$ where v is the beam velocity and c is the speed of light; X_i is the radiation length for the *i'th* material. Throughout the rest of this work the sum will be implied. This can be integrated between angular limits, θ_1 and θ_2,

$$\int I(\theta)\sin(\theta)d\theta d\phi = (e^{-\frac{X_2}{\rho_x}} - e^{-\frac{X_1}{\rho_x}}) \qquad (7)$$

where $\rho_x = \sum_i \frac{\rho_{Ai}}{X_i}$ is the areal density of an object,

$X_1 = \frac{p^2\theta_1^2}{2\times 14.1^2}$, is a characteristic areal density associated with the large polar angle limit, θ_1, and,

$X_2 = \frac{p^2\theta_2^2}{2\times 14.1^2}$, is a characteristic areal density associated with the small polar angle limit, θ_2.

Multiple lenses on a single axis, with different angular collimators, allow Coulomb radiation lengths to be separated from nuclear attenuation lengths in proton radiography.

Transmission through a single lens, including both nuclear and Coulomb attenuation, is given by,

$$I = e^{-\rho_\lambda}(e^{-\frac{X_2}{\rho_x}} - e^{-\frac{X_1}{\rho_x}}) \qquad (8)$$

The most precision can be obtained with a set of two lenses where the first is optimized to measure only nuclear attenuation by having a large aperture. If the small angle cut is zero and the large angle limit is large enough so that second term can be ignored transmission through the first lens in a two-lens system is

$$I_1 = e^{-\rho_\lambda} \qquad (9)$$

If the second lens has a large, large angle limit, but does have a small angle cut (Ferm collimator) than transmission through the second lens is given by,

$$I_2 = e^{-\rho_\lambda - \frac{X_2}{\rho_x}} \qquad (10)$$

Equations 5 and 6 can be solved for the nuclear attenuation length weighted areal densities,

$$\rho_\lambda = \ln(I_1) \qquad (11)$$

and the radiation length weighted areal densities,

$$\rho_x = \frac{1}{\ln(I_1) - \ln(I_2)} \qquad (12)$$

Hydrotest radiography requires a high energy beam to penetrate thick objects while keeping the multiple scattering angle and energy loss small enough to allow good position resolution. Proton energy of 50 GeV has been chosen for the Advanced Hydrotest Facility (AHF) to meet the design goal of 1 mm for contained shots. The multiple scattering in an armored window, projected to the center of a containment vessel gives about a 500-micron contribution to the overall system resolution with this incident beam energy.

In spite of the intellectual arguments given above, proton radiography has meet with considerable skepticism from the weapons community. This has lead to a demonstration program whose goal has been to validate these ideas. This program has had two parts: one using low energy proton beams (800 MeV) from the LANSCE accelerator at the Laboratory to perform dynamic experiments on thin systems, and the other to use high energy beams (24 GeV) from the AGS accelerator at Brookhaven to obtain static data on thick systems.

Line C

The LANSCE linear accelerator at the Laboratory provides an 800-MeV proton beam. The beam is accelerated with a micro-structure of short 100-psec-long bursts of about 5×10^8 protons every 5 ns. The beam is provided at 120 Hz in 600-μsec-long pulses. The feasibility of radiographing small (1 lb of high explosives) dynamic experiments, with a lens system, was first demonstrated at line B. For the last three years, a program of dynamic experiments has been performed on a three-lens system constructed in line C. A photograph of the line C is shown in Figure 2 below.

Several new capabilities were added to line C in the past year. Both magnetic and optical magnification were demonstrated to improve the position resolution one can obtain for on the order of 400 μm using the standard set up to as good as 100 μm by reconfiguring the two magnetic lenses to provide a single lens with a magnification of × 3. We have discovered slit collimators can be used to trade off position resolution and statistical precision independently in the x- and y-planes. Beam blockers, as opposed to collimators, were shown to provide improved density precision and dynamic range. A capability was incorporated in two experiments to look at spall layers simultaneously in the radiographs and with visor. The results were found to be in good agreement.

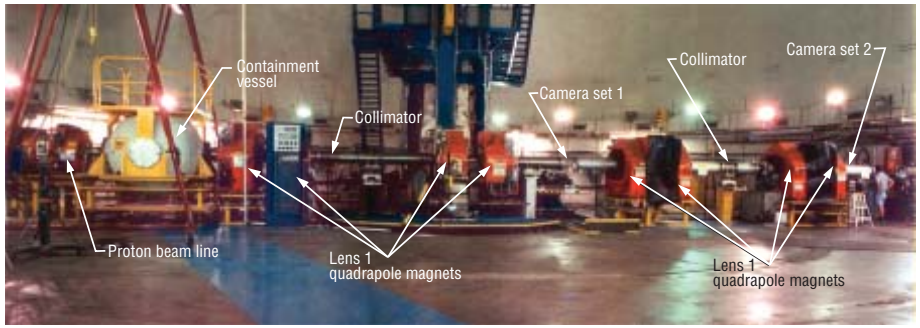

Figure 2. Photograph of the Line C proton radiography system.

Camera Developments

Significant progress has been made in developing and applying thin (<3 mm) scintillators as radiation-to-light converters to replace the lower resolution scintillating fiber-optic converters utilized in initial proton radiography efforts. The ideal, final scintillator solution has not been completed but prototype, 42-mm-square tiles with blackened edges covering a 126-mm-square field of view have resulted in high quality images with better than 2.5 lp/mm resolution and interframe times of 358 ns. Materials for these scintillators are lutetium oxyorthosilicate (LSO), yttrium oxyorthosilicate (YSO), cesium-iodine (CsI), and mixtures of inorganics. Continued development is being carried out in this area.

Efforts are ongoing to implement "4-shooter" framing cameras in order to obtain fast shuttered (<200 ns interframe times) images with good resolution (<1.5 lp/mm). We are continuing to optimize this system with upgraded charge-coupled device (CCD) readout cameras, which will result in 20 images per image plane in the near future.

The single snapshot camera system based on unique 12 KV diodes coupled to cooled CCD cameras with 1600 × 1600-pixel arrays has resulted in system resolutions better than 2.5 lp/mm. These cameras are very cost effective and have been implemented as our baseline imaging system. We continue to evaluate new, cooled CCD cameras to provide improved signal to noise, more reliable fiber optic coupling techniques, and better scene contrast. The latter is currently determined by the gated, high-voltage planar diodes.

A backthinned, 1600 × 1600 cooled CCD camera with mechanical shutter coupled to a tiled LSO scintillator was developed for experiments at the Brookhaven AGS facility to evaluate capabilities for proton radiography at 24 GeV. These results will permit extrapolation to higher energies envisioned for future proton radiography facilities.

Significant progress has been made in better defining directions for prototyping a detector system for future high energy proton radiography. Single imagers with a capability of more than 64 frames with interframe times as short as 200 ns and dynamic range in excess of 1000:1 are being targeted for a prototype utilizing photodiodes and backplane readout techniques only now reaching a maturity to permit implementation. A pixel-well capacity of >500 K is a goal to permit precision density measurements. Some work is continuing on in-proton-plane direct-conversion imagers.

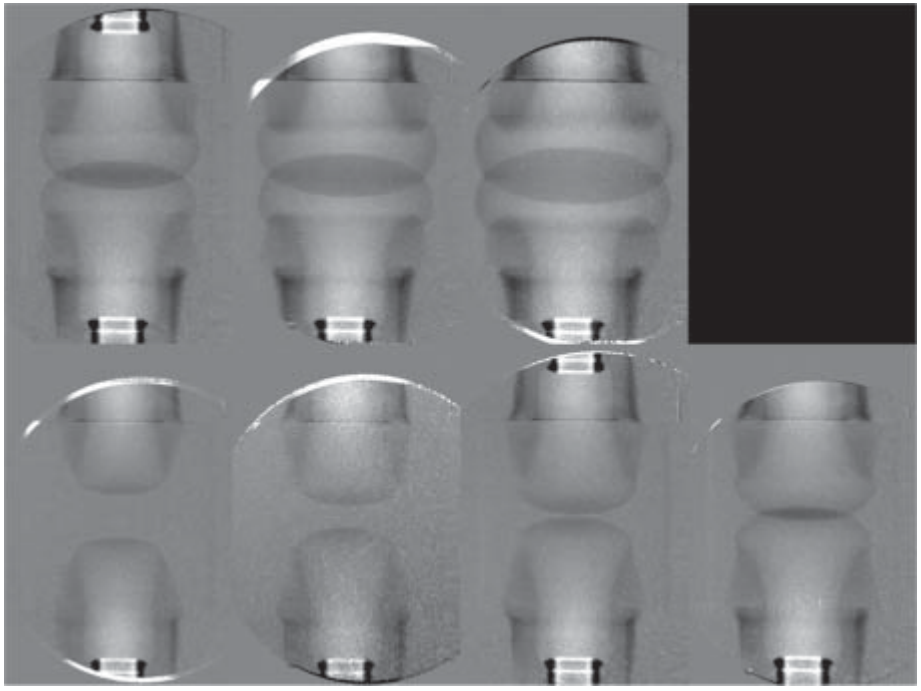

Figure 3. Radiographic sequence showing the collision of two burn fronts in PBX-9502 high explosives. The pictures are ratios of the dynamic to static radiographs. The time sequence runs from the lower left to the upper right.

Experiments

We performed 40 dynamic experiments using line C during fiscal year 2000. An additional seven experiments were performed while LANSCE was on from October until December. Thirteen of these were classified. Typically between 7 and 16 radiographs were taken for each experiment.

A number of the experiments were aimed studying detonation of high explosives. A lot of effort has been focused on the insensitive high explosive (IHE) PBX9502. Unclassified experiments were performed to measure the corner-turning properties and equation-of-state parameters for detonation products. A sequence of radiographs show the interaction of colliding detonation waves is shown in Figure 3.

Experiments aimed at studying dynamic material failure have formed an increasingly important part of the line C program. An example of an high-explosive-driven (Taylor wave) tin plate is shown in Figure 4. The failure of the tin is clearly observed in the later-time radiographs. Line out of the density distributions can be used to follow the development of the spall layers from shock break out at the tin surface. The spall of the surface was confirmed by visor data, but the radiographs provide much more data on the richness of the failure phenomena.

Figure 4. Reconstructed volume densities showing the Taylor driven (high explosive) spall of a tin plate.

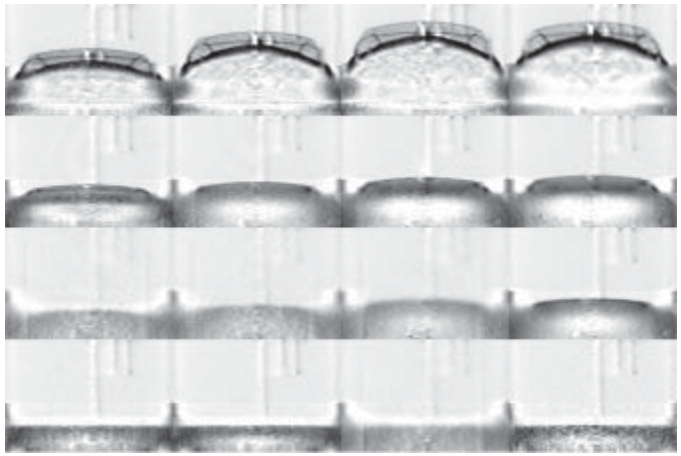

Figure 5. A view of the Experiment 933 setup looking upstream from the first camera location. The active cameras can be seen in the middle of the photograph.

AGS Data

Two experiments have been completed at the AGS using single, 40-ns-long bursts of beam line U, Experiments 933 and 955. These have demonstrated many of the features of proton radiography. A matching section and two lenses were constructed using existing refurbished 8Q48 quadrapole magnets in line U at the AGS for Experiment 933. This system was installed and commissioned using single pulses of up to 10^{11} protons at 24 GeV/c provided by the AGS. The pulse intensity was administratively limited to this value by AGS safety requirements. A picture looking upstream from the end of the second lens is shown in Figure 5.

For Experiment 955, the magnets from the two-lens system were used to construct a single shorter lens with larger angular acceptance and smaller chromatic aberrations. Data from Experiment 955 are still under analysis, so results from Experiment 933 are presented below.

Beam Characterization

Diagnostic data were obtained on a pulse by pulse basis with transformers, which measured proton fluxes at three locations in the beam line; upstream of the diffuser location, and at each of the down image locations downstream. The beam position and angle at the diffuser location were monitored using two CCD cameras looking at two phosphors, one mounted on the diffuser and one located approximately 6 m upstream of the diffuser. Combining the data from these measurements allows accurate pixel-to-pixel normalization of transmitted flux through an object to be obtained by normalizing to the measured fluxes and correcting the beam profile for shifts in position measured using the upstream images. Although preliminary analysis of the upstream data shows a correlation with the down stream beam spot location, this information was not used in the Experiment 933 analysis. However analysis of the beam data in Experiment 955 showed that this method works, indicating a similar system would have a large impact on AHF costs by removing much of the need for an upstream lens in the matching region.

The matching lens was tuned by removing the downstream collimator and installing a phosphor and CCD camera system at the collimator location. The beam was centered on the phosphor by steering it at the diffuser location and adjusting the matching quadrapoles to minimize the beam spot. The size of the beam at the collimator location corresponded to about 0.5 mrad of angle resolution at the object location. This size, which is related to the emittance of the accelerator, puts a scale on the thinnest objects that can be radiographed. The 0.5 mrad-measured resolution corresponds to about 0.85 radiation lengths or about 6 mm of tungsten. This is radiographically equivalent to having a uniform, fixed amount of material in addition to any other object that is in the beam. There was also a diffuse halo amounting to about 4% of the total beam intensity. The beam halo was eliminated in Experiment 955 by changing the beam tune. The beam tune used for Experiment 933 resulted a significant fraction of the beam intercepting an upstream magnet, producing both a halo and background. The beam emittance can be accounted for radiographically by including it in the transmission.

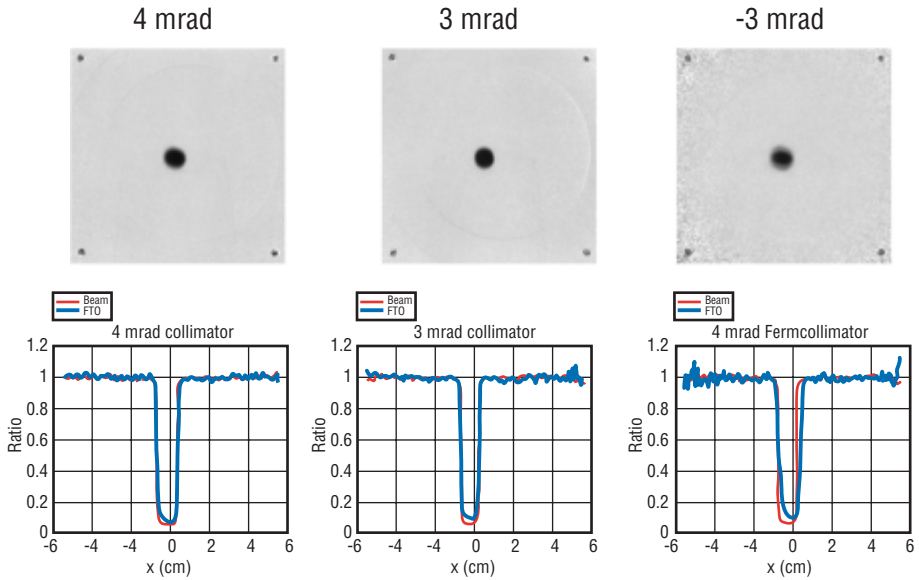

Figure 6. Top: Ratios of radiographs of the FTO with the shadow bar in to the shadow bar out for each of the collimators. Bottom: Line outs of the beam ratioed images with the shadow bar in and the FTO in in blue and with the FTO out in red.

Background Measurements

After tuning the both the matching magnets and the lens focal length, a 1 mrad collimator was installed in the upstream lens, a 1-cm-diameter, 15-cm-long tungsten rod was mounted at the object location at the beginning of the first lens, and images were made with and without the French Test Object (FTO) mounted in the object location of the second lens. The tungsten rod produces in a hole in the beam downstream of the fist lens. The background produced by each of the collimators was measured by studying how much this is filled in when an object is put in the beam with the collimator mounted in the downstream lens. The backgrounds measured from the 4.4- and 3-mrad normal and 3-mrad Ferm collimators were 2.1%, 3.9%, and 4.6% at the limb of the FTO, respectively. Although these are somewhat higher than simulations predict, they are low enough to be easily dealt with. Some of these results are displayed in Figure 6.

Position Resolution and Metrology

Position resolution and accurate metrology are important parameters for AHF applications of proton radiography. Quantitative measures of both of these parameters were obtained during Experiment 933.

The magnetic optics in the beam line and the photon optics in the detectors potentially introduce geometric distortions. These can be measured using a fiducial grid plate, shown in Figure 7.

The fiducial plate places a uniform grid of features across the entire field of view. In the acquired data, the positions of these features can be used to measure geometric distortions.

A radiograph of this object is shown in Figure 8. The expected structure is clearly visible. The data have been divided by a beam image, the position scale was offset and adjusted with a rotation and linear scaling in both x and y. The residuals for all of the intersections are potted in the rest of Figure 8. Some evidence for geometric aberrations can be seen in the residual plots. The root mean square (RMS) position error average across the entire field of view is less than 100 μm, with the largest contribution coming from the corners, where geometric aberrations are the largest.

Position resolution was measured using a resolution pattern machined into a 2.5-mm-thick piece of platinum, in both image planes. These data are shown in Figure 9. The position resolution was measured to be 250 μm full width at half maximum (FWHM) in the first image plane. A similar value was obtained in thicker classified test objects.

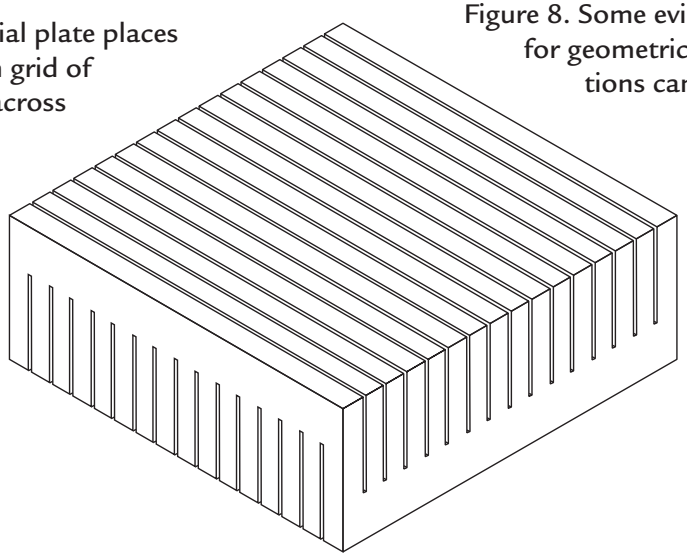

Figure 7. Fiducial grid plate. The plate is 3" thick, with perpendicular slots 2" deep cut into both faces. Each slot in the top face intersects each slot in the bottom face, forming a regular grid of square holes through the entire block.

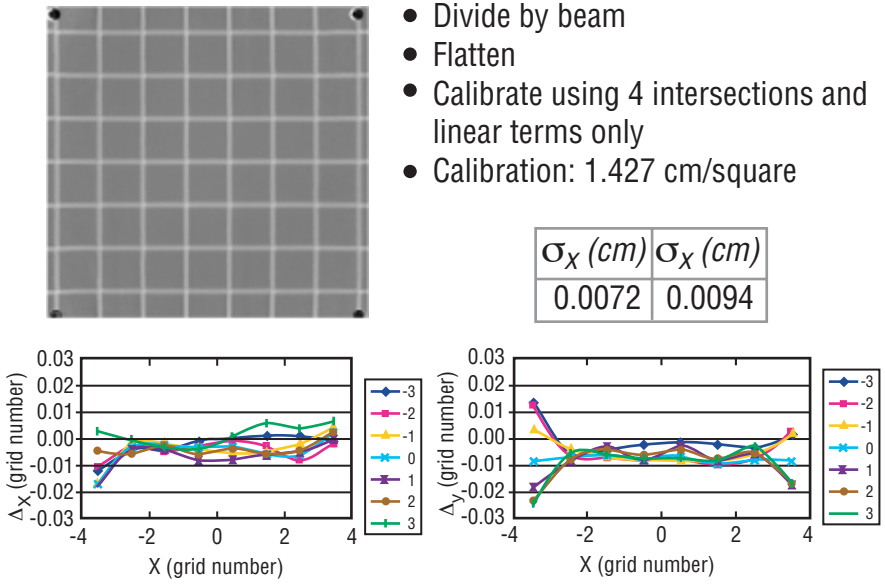

Figure 8. Radiograph and position residuals from the fiducial plate test.

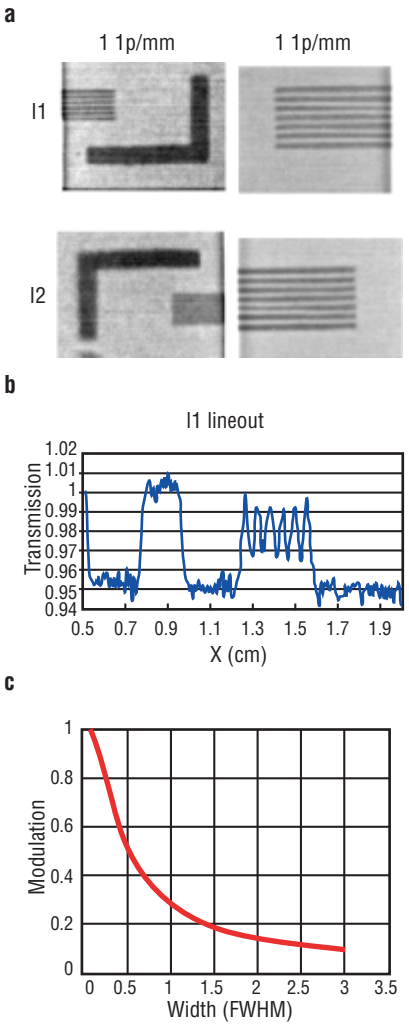

Figure 9. (a) Radiographs of the resolution test pattern. (b) Lineout of the 2-line pair/mm test pattern from image location 1,3. (c) Plot of the relationship between modulation and resolution.

Step-Wedge Measurements

After completing the lens characterization, a set of step-wedge measurements were completed on tungsten, copper, carbon and lucite, in order to provide cross sections to be used in quantitative analysis of other test objects. The finite acceptance of the beam line as a function of energy loss and scattering angle in an object can be expressed as an effective cross section, which must be known to reconstruct the density of an object from its radiograph. A simple way to measure the effective cross sections over the range of interest is to use a set of step wedges constructed from the same materials as the object and that span the thickness range of the object.

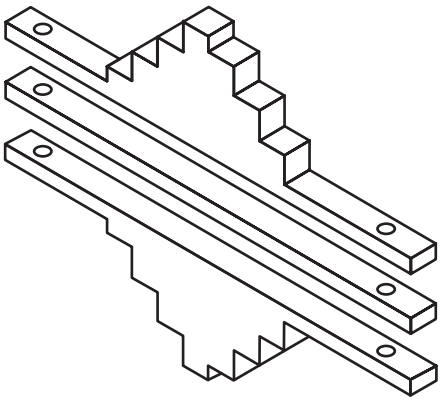

Figure 10. Doubly symmetrized step wedge. The thickness of the steps decreases on either side of center, more or less following the incident beam intensity. Using a pair of half-height wedges back to back keeps the center at a constant position and allows the insertion of spacer plates of the same material.

Figure 10 illustrates the step wedges used in Experiment 933. This design using two wedges back to back allows us to make a new configuration, a pair of wedges with small steps separated by a spacer block of the same material. This allows us to make the measurement on steps that differ by a small amount across a large range of total thickness, using only one pair of wedges. The approximate mid-plane symmetry simplifies alignment along the beam direction, and arranging the thickest part of the wedge to be in the center of the beam provides a better match of attenuation to the flux, optimizing the statistical precision of the cross section measurement for a given proton flux.

The steps in the analysis of the step-wedge data were to first align and average each of the four image plates exposed in each image plane for each picture. Four image plates were used to increase the detector quantum efficiency (DQE). Estimates made by comparing actual images with simulations suggested the resulting DQE was in the range of 20%–40%. The data from image location 1 (I1) where divided by a smoothed beam image. The results were "flattened" by fitting a two-dimensional polynomial to the regions of the picture were there was no material in the beam and then dividing the image by this polynomial. This helps to remove artifacts due to beam motion and nonuniform response of the image plates. The data from image

location 2 (I2) were taken with a Ferm collimator. These data were rotated to account for the inversion of the lens, aligned with the images from image location 1 (I1), and then divided by the I1 results. The procedure for IL1 is illustrated in Figure 11.

Cross sections were measured in steps of 1% of an attenuation length up to the full thickness of the FTO for each of the materials. Some of the results for the 10% step wedge are shown in Figure 12. The fit demonstrates the quality of quantitative agreement obtained between a semi-empirical model and the data. Step-wedge data were also taken looking through an additional 345 g/cm^2 of tungsten. These data illustrate the capability of proton radiography to obtain quantitative data over an extremely wide dynamic range of object thickness. The full set of data for I1 for the tungsten step wedge is shown in Figure 12.

The data in Figure 12 demonstrate the potential for material identification. The step wedges have been designed to cover a similar thickness range in nuclear attenuation lengths, but have a much different thickness in Coulomb radiation lengths, with the tungsten being much thicker than the carbon in

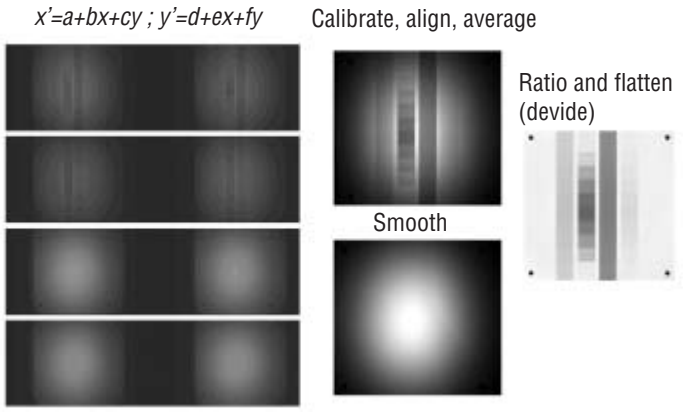

Figure 11. Images from the various steps in the analysis procedure

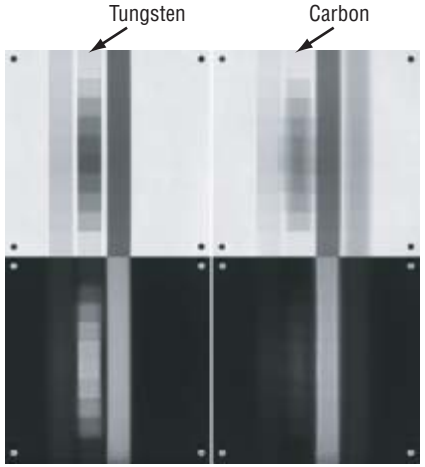

	λ (gm/cm^2)	X_0 (gm/cm^2)
Copper	124.18	14.47
Carbon	78.70	22.11
Tungsten	173.41	8.38
Lexan	74.01	18.96

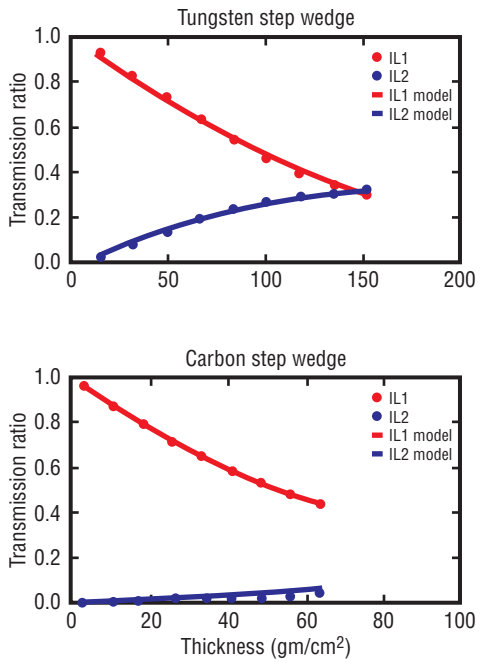

Figure 12. The carbon and tungsten 10% step wedge radiographs and data.

radiation length units. This results in much more multiple scattering in the tungsten than in the carbon. Because of this there is a dramatic difference in the I2 images, where the tungsten step wedge is clearly visible and the carbon is difficult to discern.

For thin objects, Equations 10 and 11 apply. This can be seen below where the functions of the transmission given by Equations 10 and 11 are plotted for the various 10% step wedges are plotted. The slope of these curves, which should be a measure of material type, can be seen to display the expected material dependence.

The tungsten step-wedge data span a wide range of thickness. A fit to the entire data set, assuming a Gaussian multiple scattering angular distribution and a Guassian beam emittance is shown as the solid line in the figure. The function form fitted to the flattened transmission is:

$$I = e^{-\rho_\lambda} \frac{(1 - e^{-\frac{x_1}{\rho_x + \rho_{fixed}}})}{(1 - e^{-\frac{x_1}{\rho_{fixed}}})} \qquad (12)$$

The offset, ρ_{fixed}, has been added to account for the finite beam emittance. The denominator has been added to account for the flattening, which forces the transmission to be 1 for zero thickness, even though there is some attenuation due to the beam emittance. This function can be seen to give a good account of the data over a very wide range in step wedge thickness. The fixed offset is also the reason for the nonzero intercept of the curves in Figure 13.

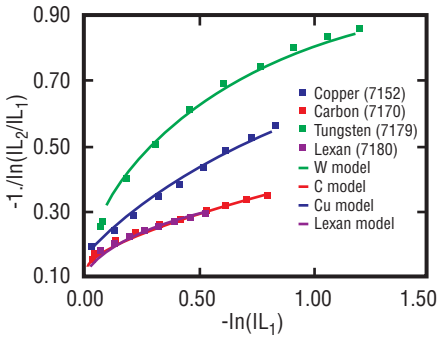

Figure 13. Plot of the functions of the transmission suggested by Equations 10 and 11 to demonstrate material identification. The materials in the step wedges are clearly distinguished by different slopes.

The approximations in Equation 12 do not work well for low-Z, thin objects because of the long tails on the beam that can be observed in Figure 6, and because of the single scattering tail on the multiple scattering angular distribution. This can also been seen by the departure from linearity for thin objects in Figure 13. The small amount of multiple scattering introduced by the low-Z step wedges results in exaggerated attenuation when it is convoluted with the tails on the beam distribution. Nevertheless the materials in the step wedges are clearly distinguished by different slopes. The effect of the angle cut in the first lens leads to the departure from linearity for the thicker steps of tungsten step wedge for which the multiple scattering cone doesn't fit within the lens acceptance.

Quantitative Density Analysis

The tungsten densities from the FTO have been reconstructed by using the data-analysis procedures similar to those outlined in the step-wedge analysis. After the four image plates were averaged, the results were divided by model radiographs of the outer foam and copper shells and then the flattening procedure was applied to the region of the radiograph outside of the tungsten region. The resulting transmission image was transformed from transmission to areal density using the same procedure as was used in the step-wedge analysis but being careful to take into account the overlying material, including the outer copper and foam shells of the FTO. The resultant areal density image was centered and volume densities were calculated using a conditioned Abel inversion method described previously.

The resultant volume densities can be compared with the measured tungsten density of 18.28 ±0.07 gm/cm^3. A histogram of the densities measured on (169 μm)^3 voxels in the region of the tungsten is shown in Figure 16. The agreement between radiographic density, and that obtained from metrology is robust and precise at the level of a percent or so. The AHF goal, driven by the criticality requirement, is to measure densities to 1%–2% in absolute precision. This result meets that goal for the simple geometry of the FTO.

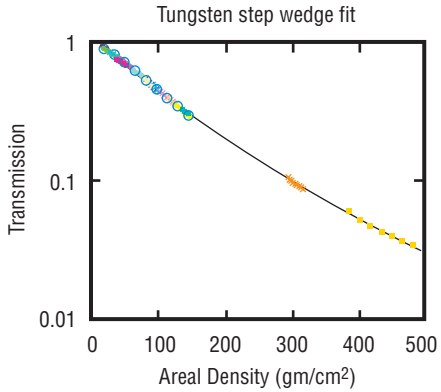

Figure 14. Image location 1 tungsten step-wedge data set. The line is a fit to the data that is used in the FTO analysis presented below.

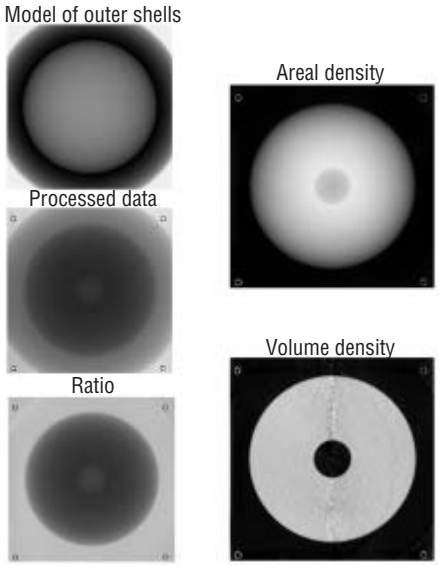

**Figure 15. (Left top) Model of outer shells
(Left middle) Measured transmission data
(Left bottom) Measured data divided by the model
(Right top) Tungsten areal density
(Right bottom) Volume density.**

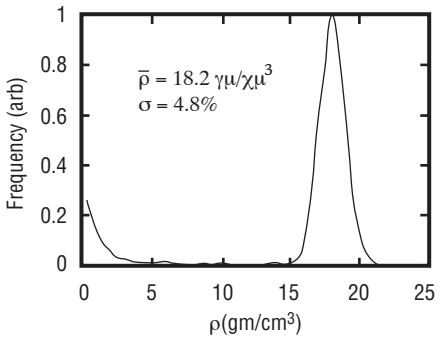

Figure 16. A histogram of radiographically measured densities in the tungsten region of the FTO. The mean value and the width are given in the figure.

Edge Resolution

The half density contour for both the inner edge and the outer edge of the FTO has been extracted and analyzed to determine the precision with which edges can be extracted from high-energy proton radiography. The AHF requirement for this quantity is 75 μm. The radius for each of the x-y pairs was extracted from the contours, and then the mean and standard deviation of these was calculated. There was no constraint on the radius of curvature and no additional smoothing beyond that from the conditioned-Abbel inversion. This analysis provides an unbiased estimate of the precision with which radii can be extracted. Limits to the precision are due to the statistical accuracy of the reconstruction (the exposure of 10^{10} protons) and by systematic sources of error such as magnetic aberrations. The contours are displayed as the red lines in Figure 17.

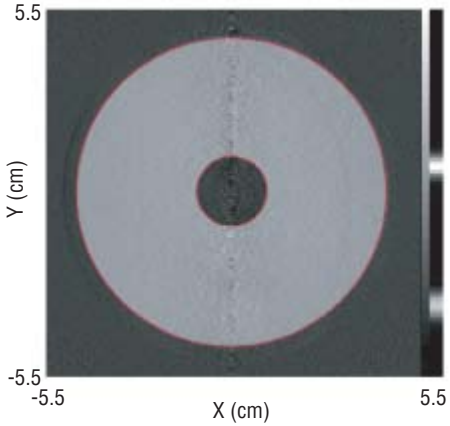

Figure 17. The red line shows the result of the contour finding routine on the volume density image from the FTO tungsten reconstruction.

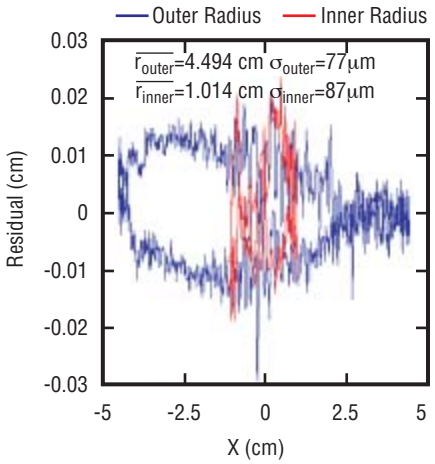

Figure 18. The residual (difference between the radius of the contour and the average radius) for the outer edge of the FTO in blue and the inner edge of the FTO in red.

The difference between the radii of the extracted contour and the average radius are plotted as a function of x in Figure 18 for both the inner radius and the outer radius. Also shown in the figure are the mean and the standard deviations averaged over the entire contour.

The average values for the measured outer and inner radii of 4.494 and 1.014 agree well with the known dimensions of the object of 4.500 and 1.000 cm respectively. However, systematic discrepancies clearly dominate the residuals. This can be seen in Figure 16 as the large correlation between the residual and x position. The random fluctuations, which are a measure of the statistical uncertainty and which impose the ultimate limit to the precision of edge determination, contribute about 30-μm to the total RMS.

Test-Object Measurements

Following this sequence of lens setup and radiographic calibration, experimental data were taken on a wide range of test objects. Some of these experiments allowed direct comparisons with DARHT, FXR and microtron x-radiography measurements. The dynamic range and sensitive of flash proton radiography were demonstrated to exceed both the current state of either flash or fixed target x-radiography in the qualitative results of all of these experiments.

Summary and Outlook

High-energy proton radiography has been shown to provide a new tool that is far superior to flash x-ray radiography. Results from the AGS at Brookhaven National Laboratory demonstrate a factor of 10–100 improvement over results obtained at DARHT on static test objects. The unique features of charged particle radiography, the ability to adjust the contrast using a collimator, to magnify the image using magnetic optics, and to provide composition dependence have all been demonstrated. The line C 800 MeV facility is continuing to be useful for making multiple-time radiographs of important dynamic experiments for Science Based Stockpile Certification.